WASP-166b: a bloated super-Neptune transiting a $V = 9$ star

Coel Hellier[1], D.R. Anderson[1], A.H.M.J. Triaud[2,3], F. Bouchy[2], A. Burdanov[4], A. Collier Cameron[5], L. Delrez[4,6], D. Ehrenreich[2], M. Gillon[4], E. Jehin[4], M. Lendl[7,2], E. Linder[8], L.D. Nielsen[2], P.F.L. Maxted[1], F. Pepe[2], D. Pollacco[9], D. Queloz[6], D. Ségransan[2], B. Smalley[1], J. J. Spake[10], L. Y. Temple[1], S. Udry[2], R.G. West[9], and A. Wyttenbach[11]

[1] *Astrophysics Group, Keele University, Staffordshire, ST5 5BG, UK*
[2] *Observatoire astronomique de l'Université de Genève 51 ch. des Maillettes, 1290 Sauverny, Switzerland*
[3] *School of Physics & Astronomy, University of Birmingham, Edgbaston, Birmingham, B15 2TT, UK*
[4] *Space sciences, Technologies and Astrophysics Research (STAR) Institute, Université de Liège, Allée du 6 Août, 17, Bat. B5C, 4000 Liège, Belgium*
[5] *SUPA, School of Physics and Astronomy, University of St. Andrews, North Haugh, Fife, KY16 9SS, UK*
[6] *Cavendish Laboratory, J J Thomson Avenue, Cambridge, CB3 0HE, UK*
[7] *Space Research Institute, Austrian Academy of Sciences, Schmiedlstr. 6, 8042, Graz, Austria*
[8] *Physikalisches Institut, University of Bern, Sidlerstrasse 5, 3012, Bern, Switzerland*
[9] *Department of Physics, University of Warwick, Gibbet Hill Road, Coventry CV4 7AL, UK*
[10] *Astrophysics Group, School of Physics, University of Exeter, Stocker Road, Exeter, EX4 4QL, UK*
[11] *Leiden Observatory, Leiden University, Postbus 9513, 2300 RA Leiden, The Netherlands*

date

ABSTRACT

We report the discovery of WASP-166b, a super-Neptune planet with a mass of 0.1 M_{Jup} (1.9 M_{Nep}) and a bloated radius of 0.63 R_{Jup}. It transits a $V = 9.36$, F9V star in a 5.44-d orbit that is aligned with the stellar rotation axis (sky-projected obliquity angle $\lambda = 3 \pm 5$ degrees). Variations in the radial-velocity measurements are likely the result of magnetic activity over a 12-d stellar rotation period. WASP-166b appears to be a rare object within the "Neptune desert".

Key words: Planetary Systems – stars: individual (WASP-166)

1 INTRODUCTION

Planets with low surface gravities have the largest atmospheric scale heights and so are the best targets for atmospheric characterisation by the technique of transmission spectroscopy, in which the planet's atmosphere is projected against the host-star photosphere during transit. Having a bloated radius also means that planets of sub-Saturn mass can still produce deep-enough transits to be found in ground-based surveys. Thus discoveries such as WASP-107b (0.12 M_{Jup}; 0.94 R_{Jup}; Anderson et al. 2017) and WASP-127b (0.18 M_{Jup}; 1.37 R_{Jup}; Lam et al. 2017) are prime targets for characterisation (e.g. Kreidberg et al. 2018; Spake et al. 2018; Palle et al. 2017; Chen et al. 2018). The importance of such targets, particularly ones transiting bright stars, will increase further with the launch of the *James Webb Space Telescope*.

Planets between the masses of Neptune and Saturn are transitional between ice giants and gaseous giants, and so could help to elucidate why some proto-planets undergo run-away gaseous accretion while others do not. There are also far fewer Neptune-mass systems known, compared to the abundance of super-Earths found by the Kepler mission, and the several-hundred transiting hot Jupiters now found by the ground-based surveys. The absence of Neptunes is particularly pronounced at short orbital periods, leading to the discussion of a "Neptune desert" (Mazeh et al. 2016).

Here we report the discovery of WASP-166b, the lowest-mass planet yet found by the WASP survey, at only twice the mass of Neptune.

2 OBSERVATIONS

From 2006 to 2012 WASP-South operated as an array of eight cameras based on 200-mm, f/1.8 Canon lenses backed by 2k×2k Peltier-cooled CCDs (see Pollacco et al. 2006 for an account of the WASP project). Each field was observed with typically 10-min cadence. The data were processed into a magnitude for each catalogued star, and the result-

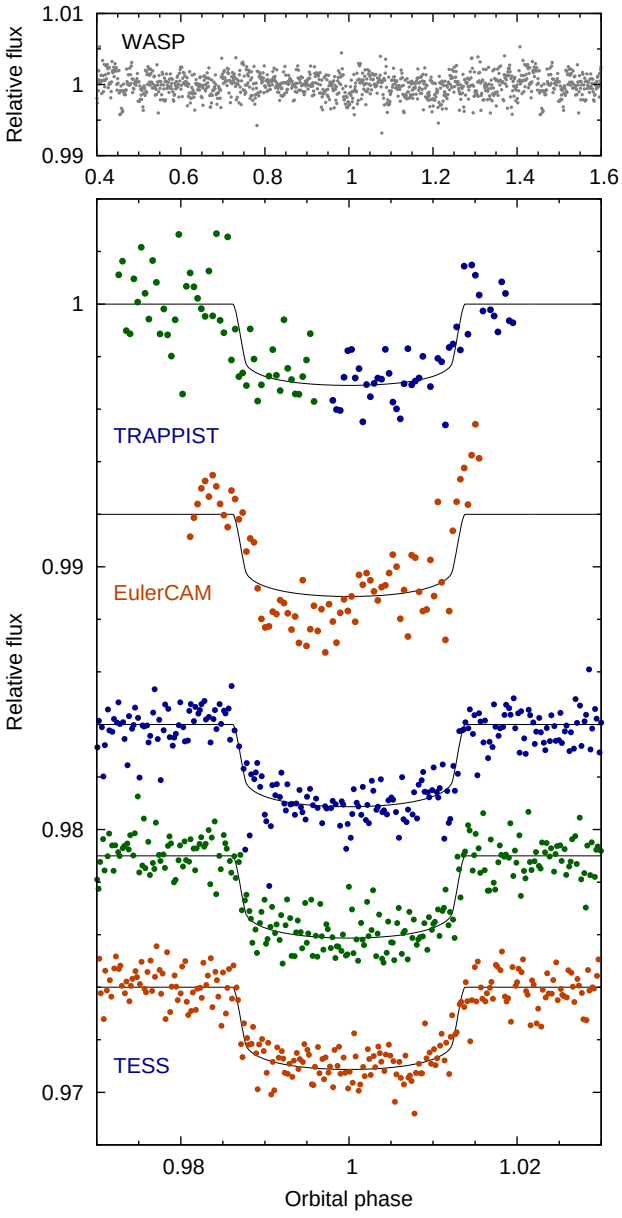

Figure 1. WASP-166b photometry: (Top) The WASP data folded on the transit period. (Main panel) Photometry from TRAPPIST-South, EulerCAM, and the three TESS transits, together with the fitted MCMC model (the TRAPPIST ingress, green points, and egress, blue points, are from different transits but are shown together).

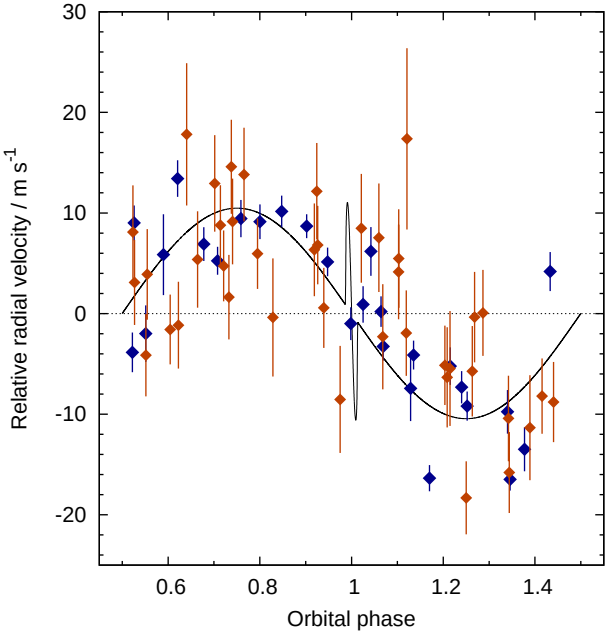

Figure 2. The HARPS (blue) and CORALIE (orange) radial velocities and fitted orbital model (the HARPS data in Fig. 4 are not shown here for clarity).

Table 1. Observations of WASP-166:

Facility	Date	Notes
WASP-South	2006 May–2012 May	33 400 points
CORALIE	2014 Feb–2017 Jan	41 RVs
HARPS (orbit)	2016 Apr–2018 Mar	27 RVs
HARPS (transit)	2017 Jan 14	75 RVs
HARPS (transit)	2017 Mar 04	52 RVs
HARPS (transit)	2017 Mar 15	66 RVs
TRAPPIST-South	2014 Mar 05	z band
EulerCAM	2016 Feb 05	I_c band
TRAPPIST-South	2016 Feb 16	z' band
TESS	2019 Feb 2–27	3 transits

ing lightcurves accumulated in a central archive. This was then searched for transit signals, with the best candidates sent for followup with the TRAPPIST-South photometer (Gillon et al. 2013) and the Euler/CORALIE spectrograph (Triaud et al. 2013). This combination has resulted in many discoveries of transiting exoplanets (e.g. Hellier et al. 2018) and the techniques and methods used here are continuations of those from previous papers.

WASP-166 was adopted as a candidate in 2014, after detection of a 5.44-d transit signal. Radial-velocity (RV) observations with CORALIE found orbital motion at the transit period, but also showed additional variations. We thus accumulated more RV data than is usual for WASP planet discoveries in order to look for additional bodies or a longer-term trend. This amounted to 41 RVs with 1.2-m Euler/CORALIE over a three-year period, and 220 RVs with the ESO 3.6-m/HARPS, of which 27 covered the orbit, while 75, 52 and 66 were taken in sequences covering transits on three different nights. The CORALIE and HARPS data were reduced using standard pipelines, as described in Rickman et al. (2019), Udry et al. (2019) and references therein.

Further photometric observations (listed in Table 1) include two partial transit lightcurves from TRAPPIST-South (one ingress and one egress) and a full transit from EulerCAM (Lendl et al. 2012), which unfortunately has excess red noise owing to poor observing conditions.

In 2019 February, after completion of the initial version of this paper, the TESS satellite observed the sky sector that includes WASP-166. TESS (Ricker et al. 2016) is performing an all-sky transit survey aimed primarily at rocky

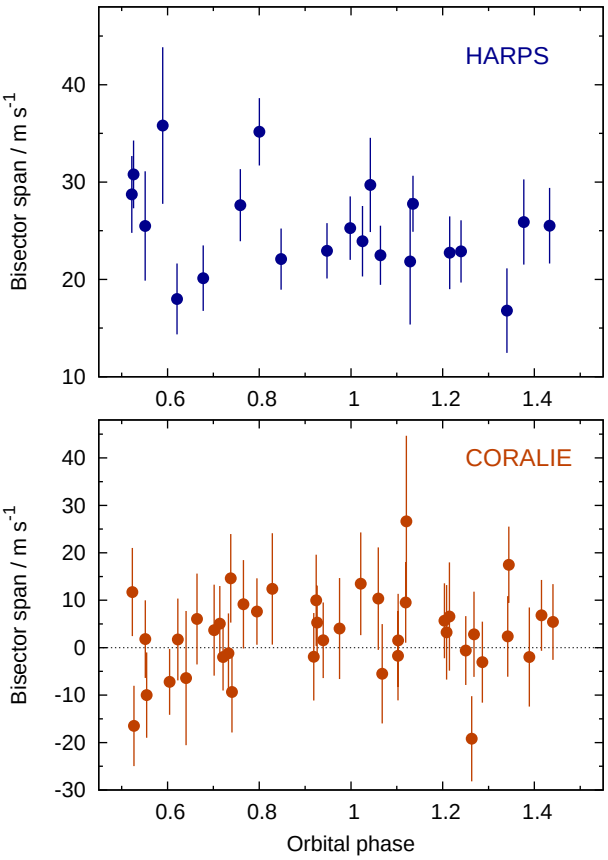

Figure 3. The spectroscopic bisector spans against orbital phase. The HARPS and CORALIE data are plotted separately since their accuracy is different. The absence of any correlation with radial velocity is a check against transit mimics.

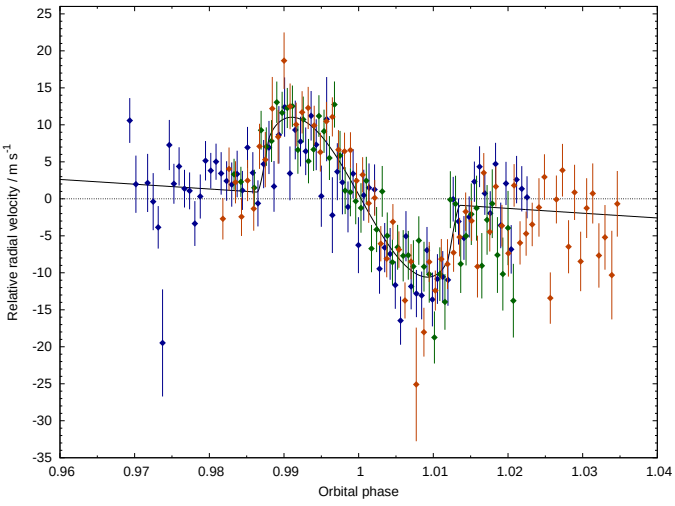

Figure 4. HARPS radial-velocity data through transit along with the fitted R–M model. The colours denote data from different nights (blue: 2017-01-14; green 2017-03-04; orange 2017-03-15).

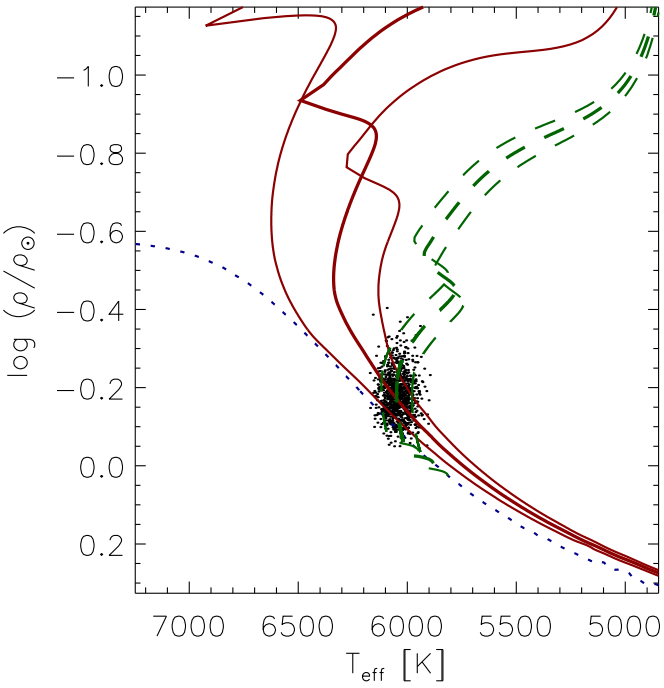

Figure 5. The host star's effective temperature ($T_{\rm eff}$) versus density (where the dots are outputs of the BAGEMASS MCMC). The blue dotted line is the zero-age main sequence, the green dashed lines are the evolutionary tracks (for the best-fitting mass of 1.18 $M_\odot$ and error bounds of 0.03 $M_\odot$), while the red lines are isochrones (for the best-fitting age of 2.1 Gyr and error bars of 0.9 Gyr).

planets too small to be found by the ground-based surveys. It has four cameras, each with a 10-cm lens backed by four 2048x2048 CCDs covering a field of 24°x24°, and observing in a bandpass from 600 to 1000 nm.

We downloaded the public TESS lightcurve for WASP-166 (= TIC 408310006 = TOI-576) from the Mikulski Archive for Space Telescopes (MAST). We used the standard aperture-photometry data products, and extracted sections of the data around the known transit times. Three transits were observed over the 25-d period (a fourth was recorded shortly after recovery from a data gap, and we discard it owing to strong out-of-transit variability).

3 SPECTRAL ANALYSIS

For a spectral analysis of the host star we combined and added the HARPS spectra and adopted the methods of Doyle et al. (2013). The resulting parameters are listed in Table 2. The effective temperature, $T_{\rm eff}$ = 6050 ± 50 K, comes from the Hα line, and suggests a spectral type of F9. The surface gravity, $\log g$ = 4.5 ± 0.1 comes from Na I D and Mg I b lines. The metallicity value of [Fe/H] = +0.19 ± 0.05 comes from equivalent-width measurements of unblended Fe I lines. The Fe I lines were also used to estimate a rotation speed of $v \sin i$ = 4.6 ± 0.8 km s^{-1}, after convolving with the HARPS instrumental resolution (R = 120 000),

Table 2. System parameters for WASP-166.

1SWASP J093930.08–205856.8	
2MASS 09393009–2058568 BD–20 2976	
RA = $09^h39^m30.09^s$, Dec = $-20°58'56.9''$ (J2000)	
V mag = 9.36; GAIA G = 9.26; J = 8.35	
Rotational modulation: < 1 mmag	
GAIA DR2 pm (RA) –55.082 ± 0.072 (Dec) 10.927 ± 0.069 mas/yr	
GAIA DR2 parallax: 8.7301 ± 0.0448 mas	
Distance = 113 ± 1 pc	
Stellar parameters from spectroscopic analysis.	
Spectral type	F9V
$T_{\rm eff}$ (K)	6050 ± 50
$\log g$	4.5 ± 0.1
$v \sin i$ (km s^{-1})	4.6 ± 0.8
[Fe/H]	+0.19 ± 0.05
log A(Li)	2.68 ± 0.08
Age (BAGEMASS) (Gyr)	2.1 ± 0.9
Parameters from MCMC analysis (fitted parameters denoted †).	
P (d)†	5.443540 ± 0.000004
$T_{\rm c}$ (TDB)†	245 7664.3289 ± 0.0006
T_{14} (d)†	0.150 ± 0.001
$T_{12} = T_{34}$ (d)	0.0088 ± 0.0012
$\Delta F^\dagger = R_{\rm P}^2/R_*^2$	0.00281 ± 0.00007
$b^\dagger$	0.39 ± 0.10
i (°)	88.0 ± 0.7
K_1 (km s^{-1})†	0.0104 ± 0.0004
γ (km s^{-1})†	23.6285 ± 0.0003
e	0 (adopted) (< 0.07 at 2σ)
a/R_*	11.3 ± 0.6
M_* ($M_\odot$)	1.19 ± 0.06
R_* ($R_\odot$)	1.22 ± 0.06
$\log g_*$ (cgs)	4.34 ± 0.05
ρ_* ($\rho_\odot$)	0.65 ± 0.10
$M_{\rm P}$ ($M_{\rm Jup}$)	0.101 ± 0.005
$R_{\rm P}$ ($R_{\rm Jup}$)	0.63 ± 0.03
$\log g_{\rm P}$ (cgs)	2.77 ± 0.05
$\rho_{\rm P}$ ($\rho_{\rm J}$)	0.41 ± 0.07
λ (deg)†	3 ± 5
$v \sin i$ (km s^{-1})	5.1 ± 0.3
a (AU)	0.0641 ± 0.0011
Irradiation (W m^{-2})	6.0 ± 0.6 ×10^5
$T_{\rm P,A=0}$ (K)	1270 ± 30
Priors were M_* = 1.18 ± 0.03 $M_\odot$ and R_* = 1.23 ± 0.06 $R_\odot$	
Errors are 1σ; Limb-darkening coefficients were:	
r band: a1 = 0.512, a2 = 0.337, a3 = –0.138, a4 = –0.015	
I band: a1 = 0.579, a2 = 0.039, a3 = 0.104, a4 = –0.101	
z band: a1 = 0.599 , a2 = –0.076 , a3 = 0.191, a4 = –0.131	

and also accounting for an estimate of the macroturbulence take from Doyle et al. (2014). We also report a value for the lithium abundance of log A(Li) = 2.68 ± 0.08.

According to Gaia DR2 (Gaia Collaboration et al. 2018), WASP-166 has a relatively high proper motion of 56 mas/yr, which at the DR2 distance gives a transverse velocity of 30.0 ± 0.3 km s^{-1}, which complements the DR2 radial velocity of 24.0 ± 0.4 km s^{-1}. WASP-166 is relatively isolated, with the nearest DR2 star being 8 arcsecs away and 9 magnitudes fainter. There is no excess astrometric noise reported (such noise can indicate an unresolved binary).

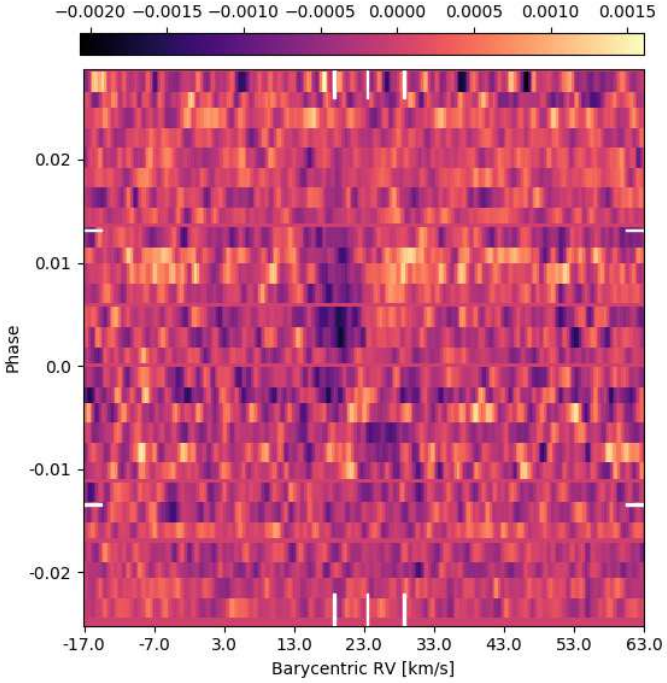

Figure 6. The line profiles through transit. The white lines show (x-axis) the mean γ velocity of the system and the $v \sin i$ line width, and (y-axis) the beginning and end of transit. The Doppler shadow of the planet moves from blue to red over the transit. The mean profile has been subtracted, resulting in a reduced level elsewhere in transit.

4 SYSTEM ANALYSIS

As is standard for WASP discovery papers, we combined the photometry and radial-velocity datasets into a Markov-chain Monte-Carlo (MCMC) analysis (e.g. Collier Cameron et al. 2007). This fits parameters including $T_{\rm c}$ (the epoch of mid-transit), P (the orbital period), ΔF (the transit depth that would be observed in the absence of limb-darkening), T_{14} (duration from first to fourth contact), b (the impact parameter) and K_1 (the stellar reflex velocity). For fitting the photometry we adopted the 4-parameter, non-linear limb darkening of Claret (2000), interpolating coefficients for the appropriate stellar temperature and metallicity.

We allowed for radial-velocity offsets between different datasets, treating the CORALIE data before and after a November 2014 upgrade, the HARPS data round the orbit, and the three HARPS transit observations, all as independent sets (the RV values are listed in Table A1). The γ velocity of the system given in Table 2 is that for the 27 HARPS datapoints around the orbit.

We adopted a zero-eccentricity fit for WASP-166b, as is usually the case for lower-mass, short-period planets. It is clear, though, that there are additional radial-velocity deviations from the fitted model; indeed the fit to the HARPS RVs around the orbit has a χ^2 of 217 for 27 datapoints. Allowing an eccentric solution did not significantly improve the fit (producing a not-significant value of $e = 0.03 \pm 0.02$, with a 2-σ upper limit of 0.07), nor did allowing a long-term drift in the RVs. Adding a second sinusoid, as could be caused by a second planet, also failed to model the ad-

ditional variability, with tells us that it is not a coherent modulation.

The MCMC process accounts for the additional RV variability, and indeed any red noise in the transit lightcurves, by inflating each dataset's errors to give $\chi^2_\nu = 1$; this balances the different datasets' influence on the final result and inflates the errors on the output parameters.

As is usual in WASP discovery papers we also constrained the stellar mass by adopting a prior based on the measured effective temperature and metallicity values, together with the stellar density obtained by an initial fit to the transit. For this we used the BAGEMASS code described in Maxted et al. (2015). This resulted in a mass estimate of 1.18 ± 0.03 $M_\odot$, and also an age estimate of 2.1 ± 0.9 Gyr. The measured lithium abundance is consistent with this age estimate, though does not constrain the age further.

Lastly, we include a constraint on the stellar radius derived from Gaia DR2 (Gaia Collaboration et al. 2018). The DR2 parallax of 8.730 ± 0.045 mas implies a distance of 113 $\pm$ 1 pc (where we have applied the correction suggested by Stassun & Torres 2018). Using the Infra-Red Flux Method (Blackwell & Shallis 1977) this implies a stellar radius of 1.23 ± 0.06 $R_\odot$, which we adopt as a prior. The initial version of this paper lacked the TESS data and so, with only limited photometry, the parameters were less secure. However, the Gaia input tied down the stellar radius, and hence the impact parameter, and thus, after including the TESS data, the values have changed by less than an error bar.

The adopted system parameters are listed in Table 2, while the data and fit are shown in Figs. 1 to 4. We also show a modified H–R diagram for the star in Fig. 5.

4.1 The Rossiter–McLaughlin effect

The above MCMC fit included fitting the in-transit radial velocities, where we use the parameterisation of Hirano et al. (2011) to model the RV deviations caused by the Rossiter–McLaughlin effect (Fig. 4). Any differences between the data on the three different nights of data could be caused by the planet crossing starspots or faculae regions.

The sky-projected obliquity angle, λ, is measured as 3 ± 5 degrees, and thus the planet's orbit is aligned with the stellar rotation. The fitted $v \sin i$ of 5.1 ± 0.3 km s^{-1} is consistent with the spectroscopic value of 4.6 ± 0.8 km s^{-1}.

In Fig. 6 we show the HARPS line profiles through transit, in a tomographic display following the methods in Temple et al. (2018). This figure shows the averaged data from all three transits, with the mean profile subtracted to better show variations. The planet trace can be seen moving prograde from blue to red over the transit. Fitting the tomogram directly (e.g. Temple et al. 2018), as opposed to fitting the modelled RVs, produces parameters consistent with those in Table 2, where again the uncertainties are currently dominated by the quality of the photometry.

4.2 Possible magnetic activity

The RV data clearly show deviations about the orbital model (Fig. 2). To illustrate this we plot in Fig. 7 some of the residual RV values as a function of time (omitting the in-transit R–M sequences). The residuals appear to be correlated from night to night.

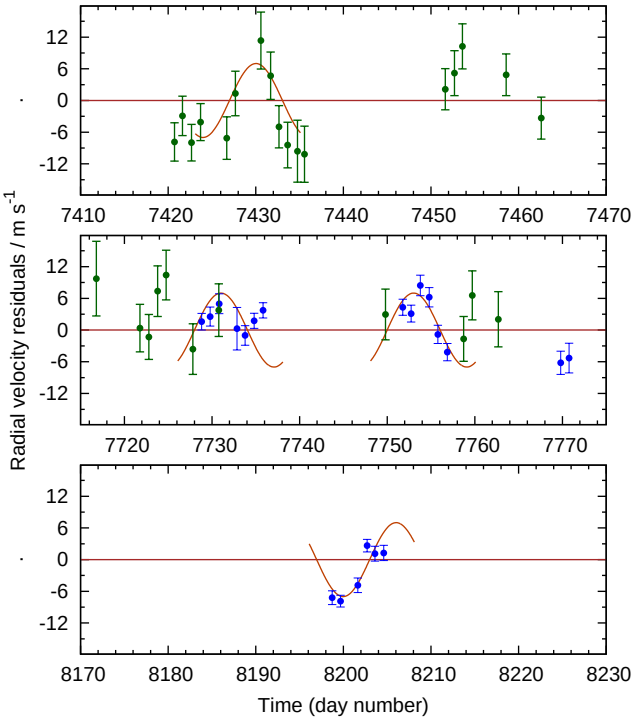

Figure 7. The residuals of the RV data to the orbital model, plotted as a function of time. Blue and green symbols are HARPS and CORALIE data respectively. The red line shows portions of sinusoid (not phase coherent) that illustrate the putative 12.1-day stellar rotation period.

Given the transit and the fact that the planet's orbit is aligned we can presume that the stellar rotation axis is perpendicular to the line of sight, and thus combining the $v \sin i$ fitted to the R–M effect with the fitted stellar radius we obtain a rotational period of 12.1 ± 0.9 days. To guide the eye we plot in Fig. 7 portions of 12.1-d sinusoid (amplitude 7 m s^{-1}), and conclude that the RV deviations might result from magnetic activity.

We have also investigated the variability by modelling the HARPS RVs using a gaussian-process (GP) analysis following the method detailed in Haywood et al. (2014). To model the residuals, this adds to the orbital motion three hyperparameters (with uniform priors), namely an amplitude a, a period $P_{\rm rot}$ (taken to be the rotational period), and an exponential decay timescale, $t_{\rm decay}$ (being the timescale on which magnetic activity would lose coherence). We set the last to $\sim$30 d, which is physically realistic, but is not constrained by the data since we have few observations separated by that timescale. The "corner plot" of the GP output is shown in Fig. 8.

The analysis produces a clear preference for a rotational period of 12.3 ± 1.9 days, consistent with that from the R–M $v \sin i$, and in line with the magnetic-activity hypothesis. The resulting values of $K_1 = 0.0100 \pm 0.0006$ km s^{-1} and $\gamma = 23.6288 \pm 0.0012$ km s^{-1} are consistent with those in Table 2.

Having found evidence of a 12-d rotational period we then searched the WASP lightcurve for any rotational mod-

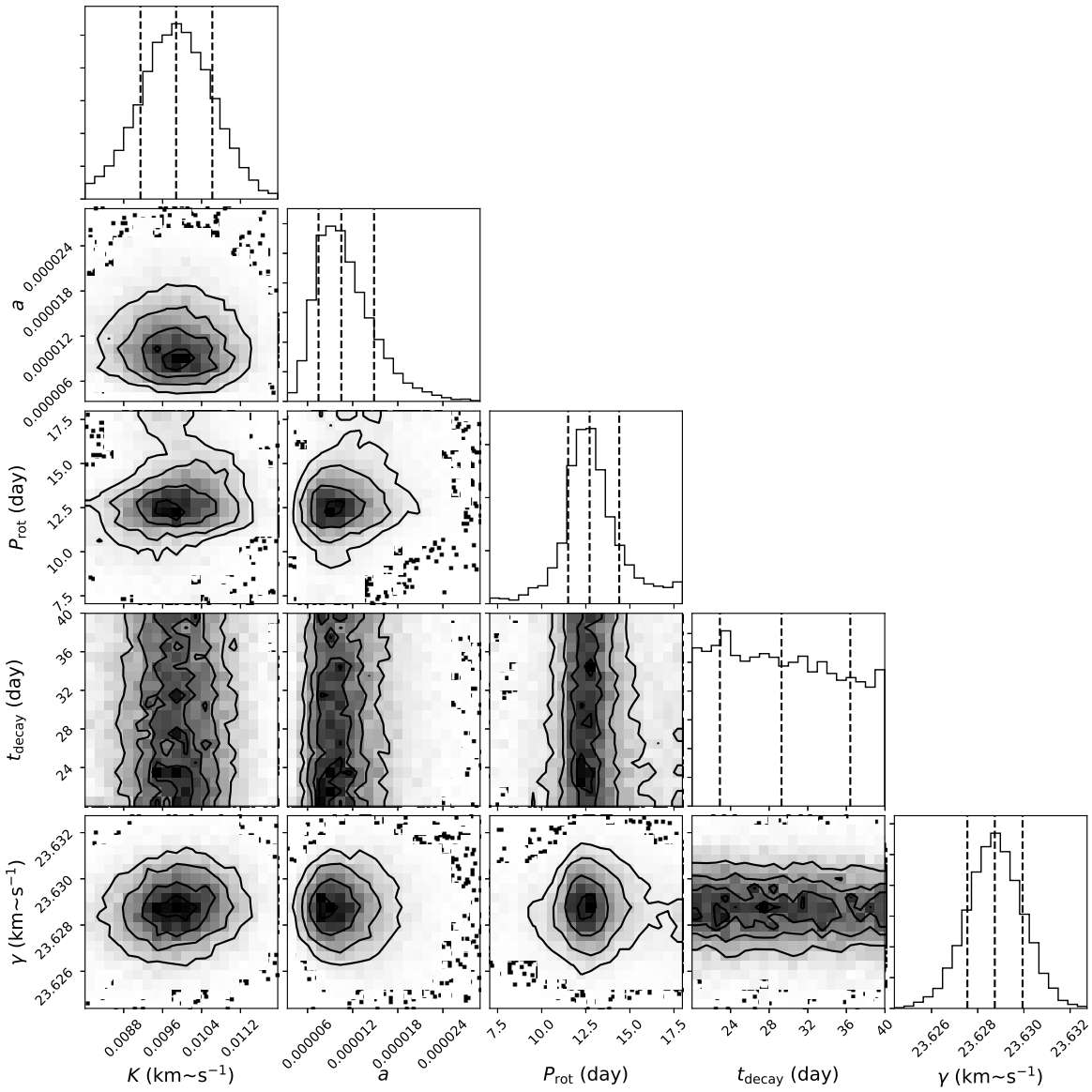

Figure 8. Parameter distributions from the gaussian-process analysis of the correlated RV residuals. The decay timescale $t_{\rm decay}$ is not constrained by the data, but there is a clear preference for a rotational period, $P_{\rm rot} = 12.3 \pm 1.9$ day.

ulation, using the methods of Maxted et al. (2011). The WASP data amount to 33 000 data points spanning ∼150 nights of coverage in each of six consecutive seasons from 2007 to 2012. We found no significant modulation to a 95% limit of 1 mmag. Given the lack of a photometric modulation, the correlated RV residuals might be attributable to magnetic suppression of photospheric convection in spot-free facular active regions (e.g. Milbourne et al. 2019).

5 DISCUSSION

With a mass of 1.9 Neptunes, WASP-166b is the lowest-mass planet yet discovered by the WASP survey. It also has a bloated radius of 0.63 ± 0.03 $R_{\rm Jup}$. The "super-Neptune" region of the mass–radius diagram for known, short-period transiting exoplanets is plotted in Fig. 9, showing that WASP-166b is near the upper size bound for a planet of its mass. The empirically observed upper bound (from WASP-127b to WASP-107b to HAT-P-26b) is falling rapidly in this mass range, which may be telling us about radius-inflation mechanisms and the ability of a lower-mass planet to hold onto its envelope under the effects of irradiation.

For example, Mazeh et al. (2016) have shown that there is a "Neptune desert" at short orbital periods, with almost no hot-Neptune planets at periods < 5 d and fewer at periods < 10 d, when compared to abundant hot Jupiters and super-Earths (see also Thorngren & Fortney 2018 on the lack of inflated sub-Saturns). To illustrate the "Neptune" or "sub-Jovian desert" we highlight the location of WASP-166b on a plot of planet mass against insolation (Fig. 10).

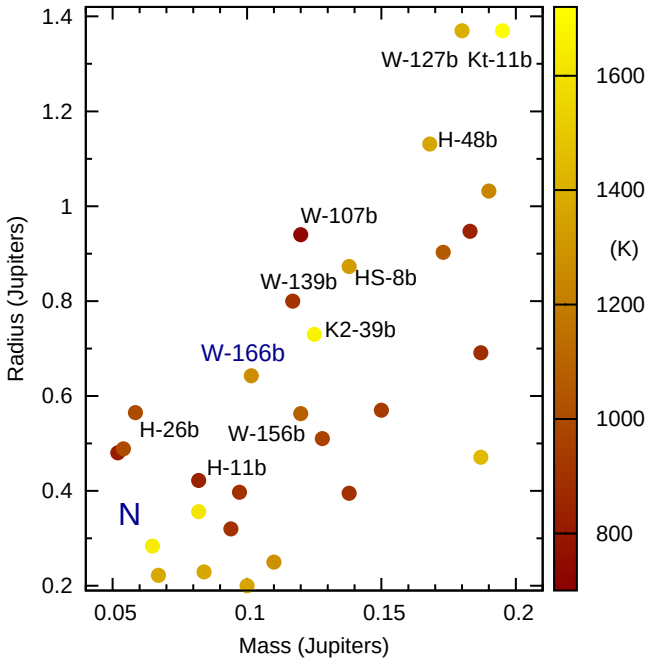

Figure 9. Masses and radii of transiting "hot" super-Neptune planets (with orbital periods < 10 d). The symbols are coloured according to the planet's equilibrium temperature. The labelled planets are WASP-107b (Anderson et al. 2017), WASP-127b (Lam et al. 2017), WASP-139b (Hellier et al. 2017), WASP-156b (Demangeon et al. 2018), HAT-P-11b (Bakos et al. 2010), HAT-P-26b (Hartman et al. 2011), HAT-P-48b (Bakos et al. 2016), HATS-8b (Bayliss et al. 2015), KELT-11b (Pepper et al. 2017) and K2-39b (Van Eylen et al. 2016; Petigura et al. 2017). The location of Neptune is marked with an N.

The desert is likely the result of photo-irradiation of inwardly migrating planets (e.g. Sestovic et al. 2018; Owen & Lai 2018; Szabó & Kálmán 2019). Jupiter-mass planets are able to resist photo-evaporation, and continue to migrate inwards by tidal orbital decay, whereas a low-surface-gravity Neptune such as WASP-166b could not. A hot Neptune could instead be captured into a short-period orbit from a high-eccentricity-migration pathway, and so, being new to its orbit, would not have undergone the photo-evaporation that would have occurred had it migrated there by the slower process of orbital decay. However, such capture only occurs for a narrow range of parameter space (Owen & Lai 2018), and so such systems would be rare.

With a period of 5.4 d and orbiting an F star, WASP-166b has a relatively high irradiation of 6×10^5 W m^{-2} (440 times Earth's insolation) for such a low-surface-gravity planet. Thus it appears to be a rare object, with a radius bloated by irradiation, on the boundary of the Neptune desert.

The Rossiter–McLaughlin observations show that the orbit is aligned ($\lambda = 3 \pm 5$ degrees). This is consistent with it being on a lengthy inwardly migration, during which it has become bloated owing to irradiation. However, recent capture from high-eccentricity pathways can also produce aligned orbits, so this is not conclusive. Relatively few of the super-Neptune planets in Fig. 9 have had obliquity angles measured, though those that have – HAT-P-11b (Bakos et al. 2010; Winn et al. 2010), WASP-107b (Anderson et al. 2017; Dai & Winn 2017; Močnik et al. 2017) and GJ 436b (Gillon et al. 2007; Bourrier et al. 2018) – are all known to be misaligned.

The bloated nature of WASP-166b combines with a bright host star of $V = 9.36$ to make it a prime target for atmospheric characterisation. Indeed, recent observations of irradiated low-surface-gravity planets show indications of photo-evaporating atmospheres (e.g. Spake et al. 2018; Mansfield et al. 2018). The expected signal for a transmission spectrum depends on the atmospheric scale height, transit depth, and host-star magnitude (e.g. equation 36 of Winn 2010). In Fig. 11 we compare the signal expected for WASP-166b with other low-mass planets ($M < 0.2$ M$_{\rm Jup}$). This shows that WASP-166b is likely to be among the best targets for such studies, though this may be more difficult if the star is indeed magnetically active, as indicated by correlated deviations in the RV data. We suggest that WASP-166b is potentially a prime target for the *James Webb Space Telescope*, and that it should first be observed with *HST* in order to assess the cloudiness of its atmosphere.

ACKNOWLEDGEMENTS

WASP-South is hosted by the South African Astronomical Observatory and we are grateful for their ongoing support and assistance. Funding for WASP came from consortium universities and from the UK's Science and Technology Facilities Council (STFC). ACC acknowledges support from STFC consolidated grant number ST/R000824/1. The Euler Swiss telescope is supported by the Swiss National Science Foundation. The HARPS data result from observations made at ESO 3.6 m telescope at the La Silla Observatory under ESO programmes 097.C-0434 and 098.C-0304. TRAPPIST-South is funded by the Belgian Fund for Scientific Research (Fond National de la Recherche Scientifique, FNRS) under the grant FRFC 2.5.594.09.F, with the participation of the Swiss National Science Fundation (SNF). The research leading to these results has received funding from the ARC grant for Concerted Research Actions, financed by the Wallonia-Brussels Federation. M.G. and E.J. are Senior Research Associates at the FNRS-F.R.S. L.D. acknowledges support from a Gruber Foundation Fellowship. This project has received funding from the European Research Council (ERC) under the European Unions Horizon 2020 research and innovation programme (project Four Aces; grant agreement No 724427). This work has been carried out in the frame of the National Centre for Competence in Research PlanetS supported by the Swiss National Science Foundation (SNSF). This paper includes data collected with the TESS mission, obtained from the MAST data archive at the Space Telescope Science Institute (STScI). Funding for the TESS mission is provided by the NASA Explorer Program. We thank the many people involved in the creation of TESS data. We acknowledge use of data from the European Space Agency (ESA) mission Gaia, as processed by the Gaia Data Processing and Analysis Consortium (DPAC).

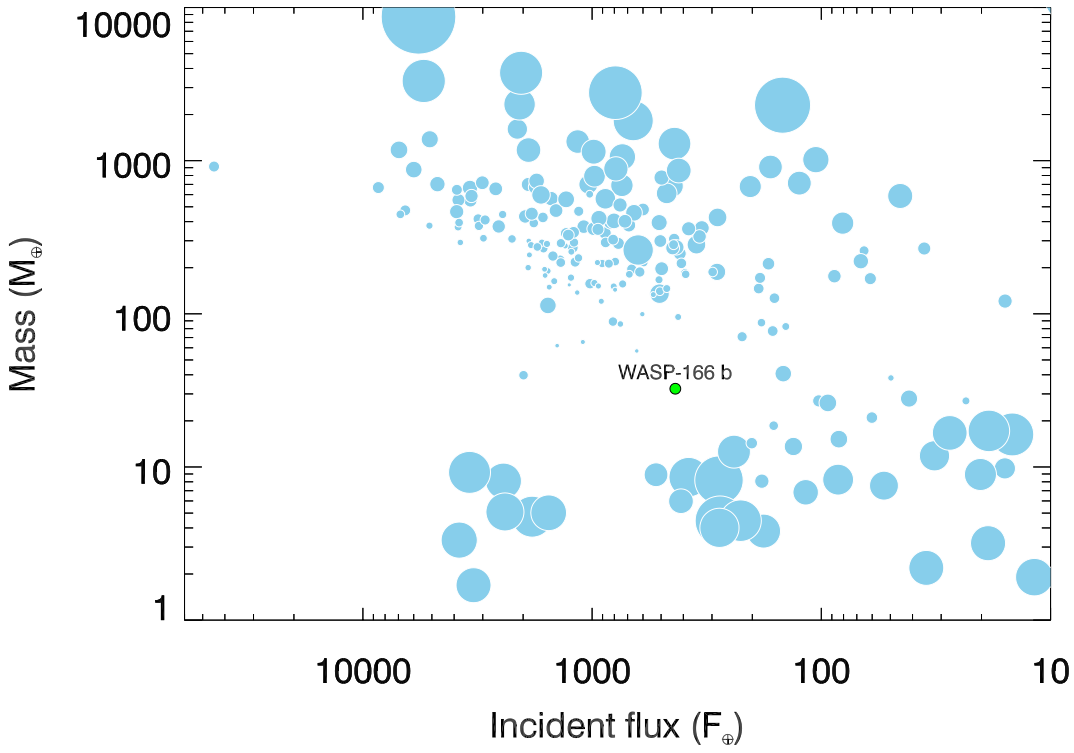

Figure 10. Exoplanet mass versus incident flux, showing the location of WASP-166b in the "sub-Jovian desert". The symbol area is proportional to the bulk density of the planet. We include only planets with host stars brighter than $V = 12$. Data are from http://exoplanets.org/

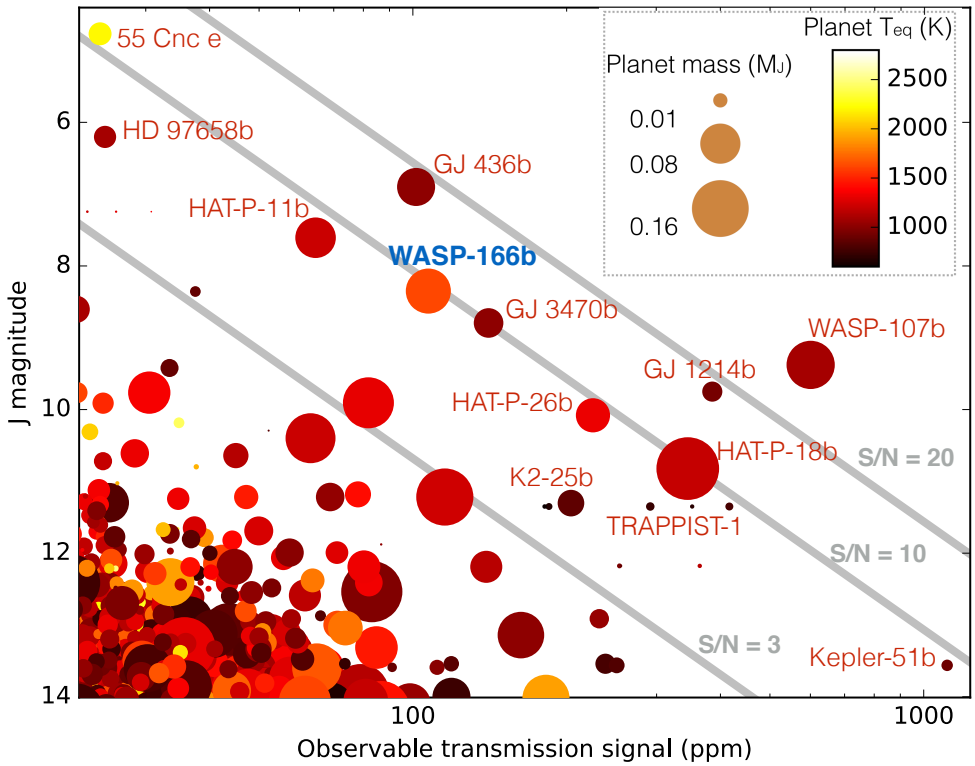

Figure 11. An illustration of prime low-mass planets (< 0.2 M_{Jup}) for atmospheric characterisation, based on the scale height of the atmosphere, the transit depth, and the host-star brightness.

REFERENCES

Anderson D. R., et al., 2017, A&A, 604, A110
Bakos G. Á., et al., 2010, ApJ, 710, 1724
Bakos G. Á., et al., 2016, preprint, (arXiv:1606.04556)
Bayliss D., et al., 2015, AJ, 150, 49
Blackwell D. E., Shallis M. J., 1977, MNRAS, 180, 177
Bourrier V., et al., 2018, Nature, 553, 477
Chen G., et al., 2018, A&A, 616, A145
Claret A., 2000, A&A, 363, 1081
Collier Cameron A., et al., 2007, MNRAS, 375, 951
Dai F., Winn J. N., 2017, AJ, 153, 205
Demangeon O. D. S., et al., 2018, A&A, 610, A63
Doyle A. P., et al., 2013, MNRAS, 428, 3164
Doyle A. P., Davies G. R., Smalley B., Chaplin W. J., Elsworth Y., 2014, MNRAS, 444, 3592
Gaia Collaboration et al., 2018, A&A, 616, A1
Gillon M., et al., 2007, A&A, 472, L13
Gillon M., et al., 2013, A&A, 552, A82
Hartman J. D., et al., 2011, ApJ, 728, 138
Haywood R. D., et al., 2014, MNRAS, 443, 2517
Hellier C., et al., 2017, MNRAS, 465, 3693
Hellier C., et al., 2018, MNRAS,
Hirano T., Suto Y., Winn J. N., Taruya A., Narita N., Albrecht S., Sato B., 2011, ApJ, 742, 69
Kreidberg L., Line M. R., Thorngren D., Morley C. V., Stevenson K. B., 2018, ApJ, 858, L6
Lam K. W. F., et al., 2017, A&A, 599, A3
Lendl M., et al., 2012, A&A, 544, A72
Mansfield M., et al., 2018, ApJ, 868, L34
Maxted P. F. L., et al., 2011, PASP, 123, 547
Maxted P. F. L., Serenelli A. M., Southworth J., 2015, A&A, 575, A36
Mazeh T., Holczer T., Faigler S., 2016, A&A, 589, A75
Milbourne T. W., et al., 2019, ApJ, 874, 107
Močnik T., Hellier C., Anderson D. R., Clark B. J. M., Southworth J., 2017, MNRAS, 469, 1622
Owen J. E., Lai D., 2018, MNRAS, 479, 5012
Palle E., et al., 2017, A&A, 602, L15
Pepper J., et al., 2017, AJ, 153, 215
Petigura E. A., et al., 2017, AJ, 153, 142
Pollacco D. L., et al., 2006, PASP, 118, 1407
Ricker G. R., et al., 2016, in Space Telescopes and Instrumentation 2016: Optical, Infrared, and Millimeter Wave. p. 99042B, doi:10.1117/12.2232071
Rickman E. L., et al., 2019, arXiv e-prints,
Sestovic M., Demory B.-O., Queloz D., 2018, A&A, 616, A76
Spake J. J., et al., 2018, Nature, 557, 68
Stassun K. G., Torres G., 2018, ApJ, 862, 61
Szabó G. M., Kálmán S., 2019, arXiv e-prints,
Temple L. Y., et al., 2018, MNRAS, 480, 5307
Thorngren D. P., Fortney J. J., 2018, AJ, 155, 214
Triaud A. H. M. J., et al., 2013, A&A, 551, A80
Udry S., et al., 2019, A&A, 622, A37
Van Eylen V., et al., 2016, AJ, 152, 143
Winn J. N., 2010, preprint, (arXiv:1001.2010)
Winn J. N., et al., 2010, ApJ, 723, L223

Table A1. WASP-166 Radial velocities.

BJD – 2400 000 (UTC)	RV (km s^{-1})	σ_{RV} (km s^{-1})	Bisector (km s^{-1})
CORALIE:			
56715.69870	23.60674	0.00420	−0.00118
56718.61401	23.60476	0.00449	0.00282
57186.46596	23.59798	0.00571	0.00657
57189.46427	23.61726	0.00466	0.00915
57379.74611	23.60818	0.00352	−0.00198
57420.73070	23.58513	0.00363	−0.00060
57421.63091	23.59524	0.00374	0.00681
57422.66015	23.60186	0.00347	−0.00721
57423.69579	23.60940	0.00350	0.00762
57426.68531	23.58764	0.00402	0.01747
57427.68034	23.60654	0.00423	−0.01649
57430.58045	23.61098	0.00540	0.01034
57431.68932	23.59771	0.00449	−0.01920
57432.65318	23.59465	0.00399	0.00542
57433.64406	23.60229	0.00431	0.00174
57434.76630	23.60306	0.00587	0.01239
57435.56404	23.59491	0.00532	0.00404
57451.62907	23.61025	0.00390	0.00528
57452.68003	23.60150	0.00425	0.00954
57453.59001	23.60351	0.00427	−0.00305
57458.58216	23.59830	0.00395	0.00568
57462.58709	23.60401	0.00398	0.00156
57488.57829	23.61223	0.00397	0.00506
57512.56673	23.62081	0.00901	0.02664
57558.45880	23.59931	0.00409	0.00181
57559.47429	23.61804	0.00467	0.01462
57560.45947	23.60978	0.00461	−0.00190
57561.46060	23.60891	0.00490	0.00154
57566.45959	23.61192	0.00541	0.01347
57568.46079	23.59210	0.00522	−0.00197
57716.80525	23.62126	0.00707	−0.00642
57721.78118	23.60734	0.00450	−0.01000
57722.79431	23.61259	0.00426	−0.00935
57723.79431	23.61560	0.00480	0.00999
57724.76502	23.60758	0.00470	−0.00170
57727.82177	23.60882	0.00479	0.00605
57730.78526	23.59711	0.00498	0.00324
57749.79985	23.61638	0.00480	0.00369
57758.72952	23.59302	0.00425	0.00237
57759.71655	23.61154	0.00464	0.01173
57762.68238	23.60114	0.00523	−0.00550
HARPS:			
57486.54275	23.61872	0.00217	0.01679
57487.53361	23.62463	0.00197	0.02873
57523.49754	23.62104	0.00324	0.02185
57526.48623	23.63539	0.00168	0.02013
57536.54610	23.63749	0.00174	0.03079
57577.46098	23.63466	0.00242	0.02971
57728.82037	23.63863	0.00157	0.02209
57729.78720	23.62939	0.00181	0.02392
57730.82154	23.62326	0.00187	0.02274
57732.85980	23.63434	0.00402	0.03581
57733.78026	23.63792	0.00185	0.02763
57734.80841	23.63362	0.00142	0.02294
57735.83008	23.62436	0.00144	0.02777
57751.77429	23.62868	0.00152	0.02248
57752.73009	23.62116	0.00160	0.02288
57753.78115	23.63266	0.00194	0.02552
57754.80284	23.64190	0.00182	0.01799
57755.78101	23.63761	0.00173	0.03517
57756.85892	23.62748	0.00163	0.02527

BJD − 2400 000 (UTC)	RV (km s^{-1})	$\sigma_{\rm RV}$ (km s^{-1})	Bisector (km s^{-1})
57767.58760	23.63394	0.00303	0.01446
57767.59207	23.62533	0.00387	0.00627
57767.60060	23.62550	0.00393	0.02186
57767.60469	23.62297	0.00386	0.00775
57767.60832	23.61950	0.00287	0.02241
57767.61151	23.60388	0.00724	0.00137
57767.61645	23.63063	0.00339	0.02259
57767.61977	23.62539	0.00270	0.02510
57767.62353	23.62773	0.00259	0.02354
57767.62751	23.62473	0.00255	0.01744
57767.63122	23.62443	0.00249	0.02932
57767.63503	23.62001	0.00303	0.03186
57767.63901	23.62367	0.00298	0.01888
57767.64282	23.62850	0.00266	0.00989
57767.64666	23.62716	0.00240	0.02489
57767.65047	23.62837	0.00244	0.02723
57767.65421	23.62679	0.00287	0.01658
57767.65819	23.62576	0.00267	0.01895
57767.66193	23.62528	0.00299	0.02379
57767.66586	23.62671	0.00315	0.02334
57767.66970	23.62449	0.00263	0.02682
57767.67342	23.63029	0.00278	0.02365
57767.67732	23.62687	0.00279	0.02616
57767.68104	23.62274	0.00312	0.02647
57767.68523	23.62805	0.00326	0.02931
57767.68907	23.63029	0.00359	0.03063
57767.69275	23.62503	0.00343	0.01836
57767.69634	23.63200	0.00388	0.01038
57767.70049	23.63575	0.00401	0.02519
57767.70436	23.62679	0.00364	0.01344
57767.70827	23.63266	0.00397	0.01581
57767.71208	23.63109	0.00336	0.01289
57767.71589	23.62978	0.00322	0.02351
57767.71979	23.63458	0.00335	0.01285
57767.72350	23.63067	0.00344	0.00116
57767.72728	23.62371	0.00414	0.01412
57767.73115	23.63412	0.00569	0.01239
57767.73531	23.62115	0.00512	0.02570
57767.73890	23.62702	0.00385	0.00477
57767.74261	23.62558	0.00432	0.03501
57767.74670	23.62226	0.00344	0.01318
57767.75044	23.62675	0.00332	0.01451
57767.75431	23.61709	0.00378	0.03052
57767.75819	23.62384	0.00345	0.03771
57767.76202	23.62485	0.00329	0.01941
57767.76605	23.62461	0.00340	0.02824
57767.76967	23.61390	0.00337	0.02390
57767.77348	23.61676	0.00333	0.02542
57767.77738	23.61591	0.00350	0.02449
57767.78119	23.61169	0.00320	0.02376
57767.78500	23.60689	0.00326	0.02685
57767.78895	23.61830	0.00339	0.02571
57767.79275	23.61151	0.00309	0.02777
57767.79656	23.61055	0.00319	0.01576
57767.80037	23.61029	0.00323	0.01117
57767.80428	23.61641	0.00314	0.01905
57767.80822	23.60975	0.00364	0.03807
57767.81189	23.61252	0.00336	0.02892
57767.81577	23.61281	0.00348	0.00388
57767.81957	23.61239	0.00349	0.01962
57767.82342	23.62330	0.00302	0.01296
57767.82726	23.62029	0.00311	0.01471
57767.83121	23.61806	0.00296	0.03654
57767.83504	23.62090	0.00278	0.01999
57767.83881	23.62567	0.00272	0.02272

BJD − 2400 000 (UTC)	RV (km s^{-1})	$\sigma_{\rm RV}$ (km s^{-1})	Bisector (km s^{-1})
57767.84263	23.62769	0.00276	0.03642
57767.84646	23.62409	0.00290	0.02824
57767.85041	23.62141	0.00297	0.02191
57767.85429	23.62807	0.00285	0.02369
57767.85802	23.61976	0.00308	0.02249
57767.86187	23.62543	0.00292	0.03571
57767.86566	23.61653	0.00328	0.01006
57767.86958	23.62595	0.00320	0.03263
57767.87338	23.62471	0.00306	0.02682
57767.87724	23.62356	0.00284	0.02180
57769.80714	23.61499	0.00219	0.02590
57770.75537	23.62649	0.00281	0.02549
57816.65537	23.63019	0.00210	0.02144
57816.66032	23.62917	0.00204	0.01473
57816.67017	23.62837	0.00244	0.01715
57816.67507	23.63615	0.00262	0.01374
57816.67886	23.63392	0.00261	0.02071
57816.68266	23.63469	0.00283	0.01612
57816.68652	23.63993	0.00280	0.01991
57816.69042	23.63850	0.00285	0.02664
57816.69419	23.63915	0.00271	0.02256
57816.69791	23.63940	0.00279	0.01625
57816.70188	23.63349	0.00323	0.03297
57816.70578	23.63760	0.00310	0.02489
57816.70961	23.63197	0.00300	0.01579
57816.71334	23.63354	0.00289	0.01285
57816.71721	23.63807	0.00281	0.02084
57816.72097	23.63601	0.00292	0.02362
57816.72490	23.63239	0.00297	0.01569
57816.72856	23.63962	0.00312	0.01805
57816.73260	23.63272	0.00334	0.01253
57816.73633	23.62798	0.00317	0.02418
57816.74019	23.62777	0.00325	0.02878
57816.74404	23.62656	0.00312	0.02588
57816.74787	23.62564	0.00335	0.03502
57816.75177	23.62932	0.00324	−0.00833
57816.75556	23.62015	0.00320	0.03667
57816.75929	23.62272	0.00305	0.03631
57816.76336	23.62788	0.00344	0.02356
57816.76706	23.62189	0.00314	0.01721
57816.77082	23.61831	0.00307	0.04728
57816.77461	23.62033	0.00303	0.01428
57816.77864	23.61918	0.00347	0.03644
57816.78237	23.61925	0.00330	0.03297
57816.78610	23.61773	0.00355	0.02491
57816.79007	23.62124	0.00328	0.02607
57816.79383	23.61770	0.00337	0.02593
57816.79766	23.61668	0.00384	0.03799
57816.80145	23.60814	0.00352	0.02619
57816.80537	23.61670	0.00362	0.02351
57816.80909	23.61294	0.00376	0.02974
57816.81303	23.62676	0.00385	0.01295
57816.81682	23.62619	0.00381	0.01807
57816.82062	23.61808	0.00393	0.02724
57816.82449	23.62186	0.00398	0.03071
57816.82832	23.62480	0.00416	0.02181
57816.83212	23.62562	0.00439	0.02305
57816.83599	23.61783	0.00442	0.00742
57816.83982	23.62403	0.00471	0.02442
57816.84358	23.62622	0.00465	0.01361
57816.84738	23.61928	0.00512	−0.00844
57816.85131	23.61671	0.00493	0.02648
57816.85511	23.62293	0.00502	0.02198
57816.85898	23.61311	0.00498	0.00126

BJD − 2400 000 (UTC)	RV (km s^{-1})	$\sigma_{\rm RV}$ (km s^{-1})	Bisector (km s^{-1})
57827.53425	23.62930	0.00280	0.02204
57827.53872	23.63603	0.00290	0.02670
57827.54345	23.63423	0.00285	0.02590
57827.54786	23.62957	0.00259	0.02816
57827.55227	23.63447	0.00278	0.01389
57827.55676	23.63066	0.00297	0.02514
57827.56098	23.63909	0.00305	0.02265
57827.56519	23.63729	0.00373	0.02886
57827.57028	23.64419	0.00428	0.02696
57827.57457	23.64038	0.00364	0.02522
57827.57890	23.65067	0.00382	0.02796
57827.58327	23.64449	0.00309	0.02050
57827.58769	23.64204	0.00295	0.02194
57827.59202	23.64369	0.00286	0.03653
57827.59643	23.64428	0.00285	0.02834
57827.60084	23.64191	0.00267	0.03241
57827.60533	23.63830	0.00263	0.01467
57827.60976	23.64247	0.00262	0.02718
57827.61409	23.64307	0.00264	0.01784
57827.61850	23.63863	0.00266	0.04245
57827.62295	23.63842	0.00252	0.01951
57827.62728	23.63858	0.00241	0.02096
57827.63170	23.63444	0.00238	0.02134
57827.63615	23.63524	0.00238	0.01689
57827.64056	23.63139	0.00264	0.01744
57827.64497	23.63212	0.00243	0.02347
57827.64938	23.62593	0.00239	0.02557
57827.65372	23.62390	0.00251	0.02587
57827.65821	23.62888	0.00241	0.02687
57827.66262	23.62513	0.00246	0.02387
57827.66703	23.61826	0.00244	0.03302
57827.67144	23.62351	0.00237	0.01251
57827.67526	23.60691	0.00768	−0.01366
57827.68085	23.61397	0.00330	0.02234
57827.68469	23.62346	0.00271	0.01181
57827.68917	23.61960	0.00271	0.01719
57827.69354	23.62385	0.00272	0.01891
57827.69801	23.62317	0.00337	0.03128
57827.70243	23.62472	0.00259	0.02089
57827.70685	23.62682	0.00261	0.01774
57827.71126	23.63026	0.00259	0.02072
57827.71559	23.62902	0.00272	0.00473
57827.71986	23.62284	0.00418	0.02883
57827.72448	23.63551	0.00267	0.03343
57827.72884	23.62753	0.00266	0.02473
57827.73326	23.63365	0.00270	0.02559
57827.73771	23.62836	0.00282	0.02362
57827.74242	23.62463	0.00315	0.02299
57827.74657	23.63381	0.00288	0.02348
57827.75090	23.62604	0.00292	0.01722
57827.75536	23.62729	0.00298	0.03213
57827.75977	23.62853	0.00294	0.02042
57827.76467	23.63083	0.00395	0.02306
57827.76868	23.63494	0.00308	0.04233
57827.77297	23.61858	0.00347	0.02458
57827.77742	23.63191	0.00324	0.01560
57827.78183	23.63586	0.00356	0.01705
57827.78629	23.62552	0.00359	0.02208
57827.79066	23.63287	0.00373	0.01926
57827.79507	23.62353	0.00402	0.02713
57827.79944	23.63074	0.00404	0.02189
57827.80389	23.63272	0.00406	0.01771
57827.80837	23.62434	0.00435	−0.00767
57827.81284	23.62679	0.00437	0.02713
57827.81780	23.62169	0.00599	0.03090
57827.82180	23.63132	0.00444	0.01595

BJD − 2400 000 (UTC)	RV (km s^{-1})	$\sigma_{\rm RV}$ (km s^{-1})	Bisector (km s^{-1})
58198.71811	23.61212	0.00130	0.02011
58199.67572	23.61200	0.00111	0.02893
58201.64627	23.63373	0.00139	0.02105
58202.70438	23.63717	0.00119	0.01943
58203.61226	23.62522	0.00141	0.01834
58204.60885	23.61929	0.00145	0.02213

Bisector errors are twice RV errors. Lines denote an instrument upgrade, or separate through-transit sequences